EUROPEAN ORGANIZATION FOR NUCLEAR RESEARCH

CERN/PPE 91–7 Rev.
16 January 1991

CM-P00062753

# DEVELOPMENT OF A FAST RICH DETECTOR USING A MWPC AT LOW GAIN WITH PAD READOUT AND A NaF RADIATOR

F. Piuz[1], R.S. Ribeiro[4], T. Francke[5], P. Martinengo[3], M. Suffert[2] and T.D. Williams[1]

1 CERN, European Organization for Nuclear Research, Geneva, Switzerland.
2 CRN, Centre de Recherches Nucléaires, Strasbourg, France.
3 Genova University, Genova, Italy.
4 LIP, Laboratório de Instrumentação e Física Experimental de Particulas,Coimbra, Portugal.
5 Manne Siegbahn Institute, Stockholm, Sweden.

**E R R A T U M**

Please find enclosed a new revised version of this paper, since:

(a) a mistake has happened about fig. 19 (page 19), which has now been replaced by the correct one (the legend is the same);

(b) some other little amendments have been applied on page 5 (legend of fig. 3) and page 10 (legend and top row of table 1).

## ABSTRACT

We present the study of a fast RICH detector with a proximity focusing geometry constituted of a solid radiator (NaF) and a symmetric MWPC of 4 mm thickness as a photodetector. Photo-electrons and particles are localized by measuring the charges induced at a cathode segmented into pads of $8 \times 8$ mm$^2$, with the help of a VLSI electronics. Using TMAE at 30 – 50°C in a 95 methane/5 isobutane mixture, up to 24 electrons per ring are detected (factor of merit of 58 cm$^{-1}$), at a chamber gain not larger than $5 \times 10^4$. An accuracy of 1.3 mm on the Cherenkov ring radius is achieved. These results are compared to a simulation model for physical evaluation of the detector behaviour: feedback photons, quantum efficiency, separation power, etc.

Presented at the Experimental Apparatus for High-Energy Particle Physics and Astrophysics Conference, 28 May – 1 June 1990, San Miniato, Italy

# 1. INTRODUCTION

Results have recently been reported [1] about the performances of a fast RICH detector having, as the photon detector, a thin MWPC with a two-dimensional pad structure readout by means of a VLSI electronics. TEA was used as photo-converting vapour, to take advantage of a room temperature operation without feedback photons problems. 20–30 pads (size $8 \times 8$ mm$^2$) hit per ring were recorded at a chamber gain of $\approx 2 \times 10^5$. However, in the prospect of the production of a large detecting area, these attractive features of TEA are balanced by technical implications, such as the need of costly $CaF_2$ windows inherent to the quantum efficiency range of this vapor.

A well known alternative to this problem is the use of TMAE vapour, the higher quantum efficiency of which yields to the conversion of more photons, at energies permitting the use of quartz windows. However, the inconvenient is now the large mean-free path of photon absorption in TMAE at room temperature, $\lambda_a$. It is seriously conflicting with the many reasons imposing the use of a MWPC as thin as possible, such as larger-induced signals, small energy deposit of the charged particle and small parallax error at the point of photo conversion. Therefore, balance should be found between the TMAE temperature operation, which reduces $\lambda_a$, and chamber gain and pad geometry to keep to a minimum the inefficiency in detecting photo-electrons and the expected yield of feedback photons in a chamber without "blinds". That will be the points under study in this paper, having in mind the care of achieving a large-size detector of easy and cheap manufacturing. With the same goal, the question of the accuracy on the ring radius, bound to the pad size, that is, to their number, will be examined.

# 2. MEASUREMENTS

## 2.1 Detector set-up, electronics and operation

As shown in fig. 1, Cherenkov photons are emitted along the path of a charged particle in a 10 mm thick NaF plate. Then, they traverse a gap filled with helium to enter the detector through a quartz window (Suprasyl II, 3 mm thick) and the first cathode made of a stainless-steel mesh pressed against it (500 μm □,50 μm). The transparency of this ensemble is evaluated later on. The MWPC has a half gap of 2 mm, sense wires are spaced by 4 μm, 20 μm in diameter, 400 mm long, and the pad size is of $8 \times 8$ mm$^2$.

The pad cathode is made of two printed boards glued on both sides of a foam plate, 10 mm thick. The pad structure is etched on the inner circuit. The problem of connecting in a tight and short way every pad to its preamp is a non-trivial one when a small amount of material is requested together with a good flatness and accessibility to the electronics. Our chamber was not optimized in order to achieve a minimum amount of matter; however,

prototype electrodes of 0.50 $m^2$ (8000 pads) are under construction, representing $\leq 2\%$ of an interaction length (electronics included), and a flatness of $\leq \pm 50$ μm, adequate for a safe gain uniformity at our working gap thickness.

A second radiator configuration (fig. 1(b)), which allows an even more compact detector array, was tested with similar performances than the first one.

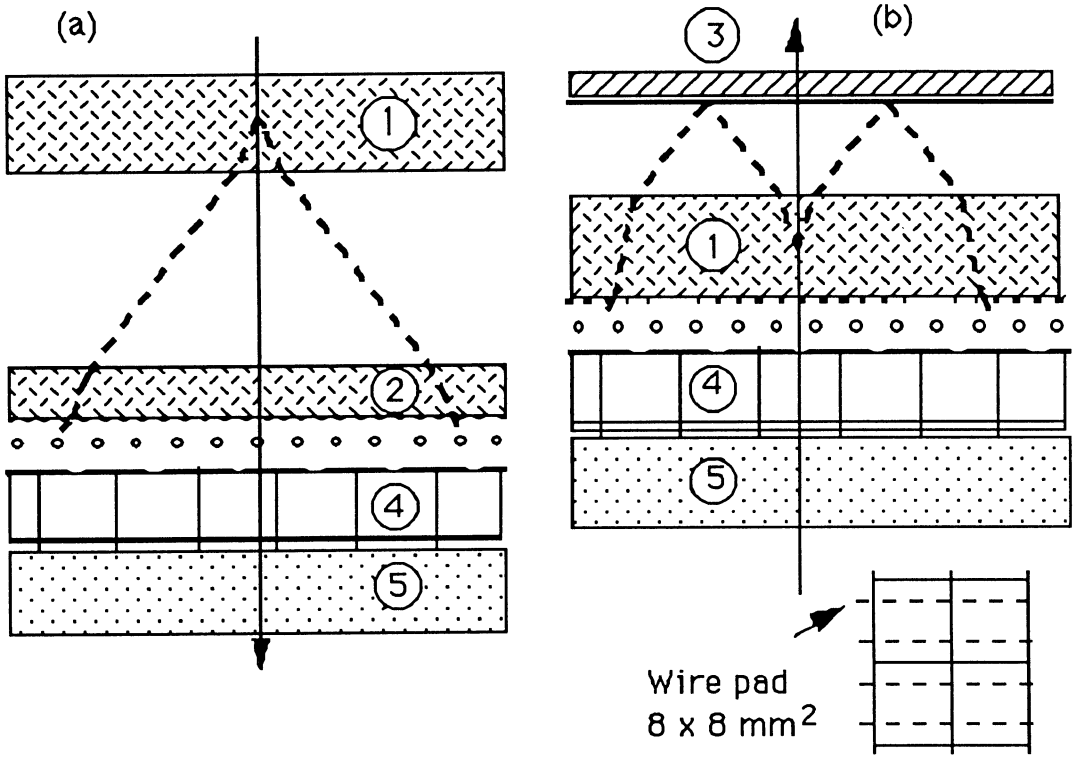


**Fig. 1** Scheme of the detector layout. The helium gap is adjustable in order to achieve a ring radius smaller than 40 mm (or smaller) at any particle and momentum choices. (1) radiator, (2) window, (3) mirror, (4 and 5) pad electrode and electronics. The arrow indicates the particle trajectory.

Every pad was connected to an analog multiplexed readout electronic chain, already described in ref. [1]. Its components are the front-end VLSI CMOS chip AMPLEX [2] associated to the readout card DRAMS [3]. The characteristic performances of this chain are a mean-noise figure of 0.18 fC r.m.s., a minimum threshold of detection of 0.4 fC and a linear dynamical range of 70 fC (0.1 fC = 625 electrons equiv. charge). As a DRAMS operates with an 8-bit digitization, we shall use in the following text and figures an "ADC ch.", that is 0.3 fC, as a unit of charge.

The gas in use was a mixture of 95% methane and 5% isobutane passing through a TMAE bubbler at variable temperature, the detector and tubings being maintained 5–10°C higher.

The detector was installed at a CERN/PS test beam, T11, providing a mixture of protons and pions at momenta of 0.8 to 3.5 GeV/c. A time of flight (TOF) system was

used for particle identification at the software level. The event definition was set by the coincidence of scintillators defining an area of $10 \times 10$ mm$^2$ in the centre of the zone of equipped pads, $96 \times 96$ mm$^2$ or 144 pads. Two translations and rotations of the chamber allowed the study of inclined tracks.

## 2.2 Results of the measurements at the test beam

The properties of the detector were studied, varying by: (i) the TMAE/chamber temperature from 30 – 50°C, (ii) the chamber gain, anode voltage 1700 to 1850 V, (iii) the beam momentum, and (iv) the track inclination.

Events are characterized by $N_{pad}$, the number of pads delivering a signal above a fixed electronic threshold. In case of a Cherenkov ring, this number is different from the number of photo-electrons because several of them can induce a signal at the same pad, as the maximum ring radius is limited at $\approx 40$ mm.

Figure 2 shows an example of a ring pattern with the central impact of the particle. Selecting pions of $\beta \approx 1$ and a large helium gap, allows to evaluate the mean number of pads hit by the charged particle (MIP) in absence of Cherenkov photo-electrons in the sensitive pad region.

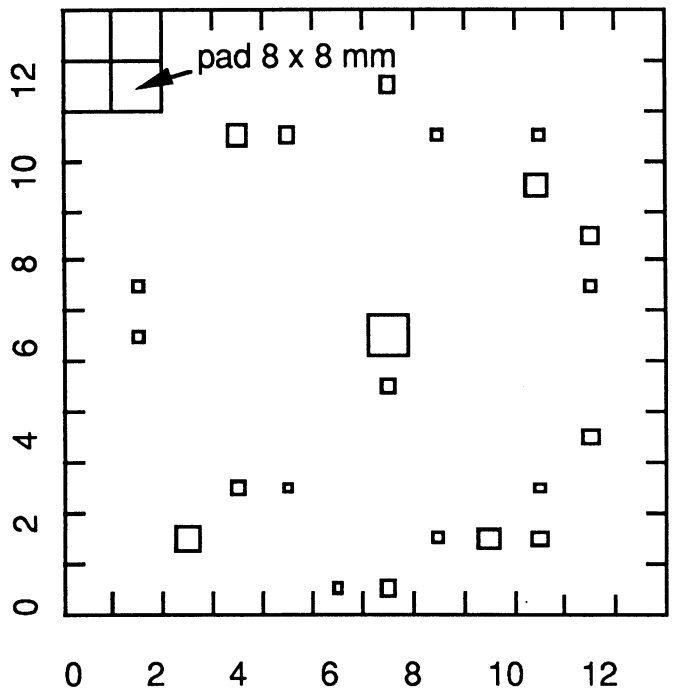


**Fig. 2** Example of the pad pattern of a single event. The size of the picture frame is of $12 \times 12$ pads of $8 \times 8$ mm$^2$. The square area is proportional to the pulse height. Photo-electrons and MIP are seen well separated. Proton $\beta = 0.84$; HV = 1750 V, TMAE at 50°C, pad threshold = 2 ADC ch, ring radius = 35 mm.

A number < 5 pads/MIP is found at our highest gain and TMAE temperature (fig. 3). The number of accompanying hits detected far from the impact is then < 2/MIP. The threshold was kept at its minimum value.

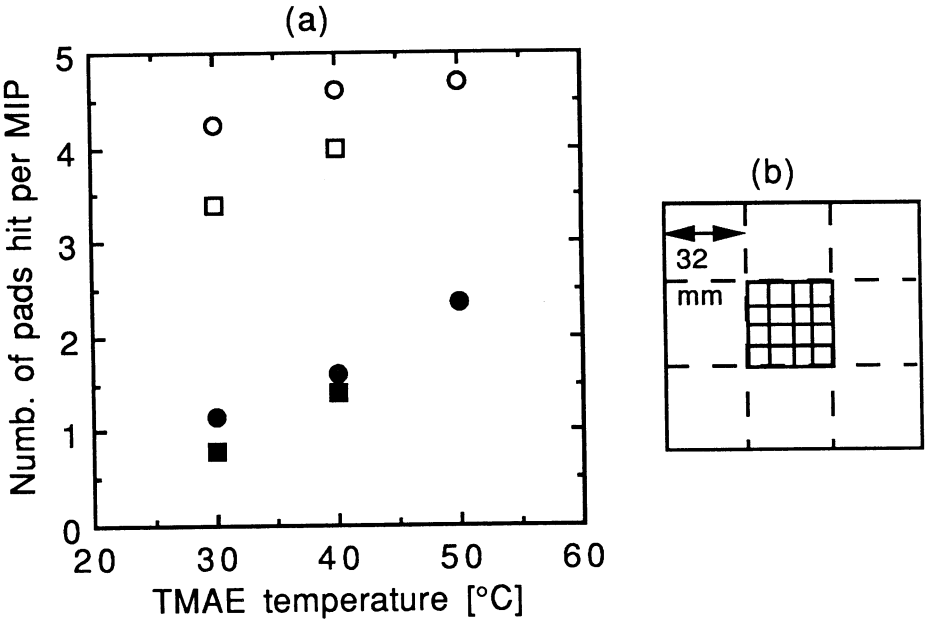


**Fig. 3** (a) Dependence of the mean number of pads hit/MIP inside (open symbol) and outside(full symbol) the central zone versus TMAE temperature and chamber gain. Square: 1750 V, circle: 1800 V, pion $\beta = 0.995$.
(b) Scheme of the central "beam" zone.

Figure 4 shows two distributions of $N_{pad}$ obtained at a ring radius of 35 mm, having excluded the central 16 pads where the MIP hits are. These distributions have a symmetrical shape, with mean values as high as 35 pads hit per ring, while a MIP distribution has a typical Landau profile. Pulse height spectra are shown later on in case of photo-electrons.

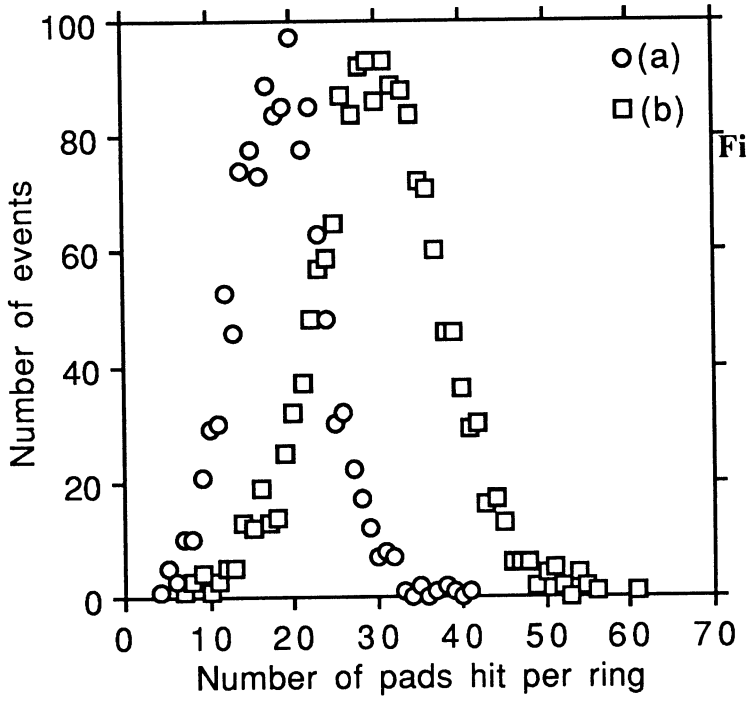


**Fig. 4** Two distributions of $N_{pad}$, the mean number of pads hit/ring (no MIP):

(a) protons $\beta = 0.966$, HV = 1700 V, TMAE at 40°C, pad threshold 2 ADC ch, ring radius of 35 mm.
(b) HV = 1750 V, TMAE at 50 °C.

The evaluation of a ring radius is taken as the average of the distances between the centre of every pad hit in this ring and the MIP impact, obtained as an analog centroid of the MIP pad hit pattern. That is equivalent, in fact, to a "digital" centroid finding. A distribution of such radii is shown in fig. 5. The r.m.s. of the Gaussian fit is 1.3 mm at $\beta = 0.96$ (see also fig. 17).

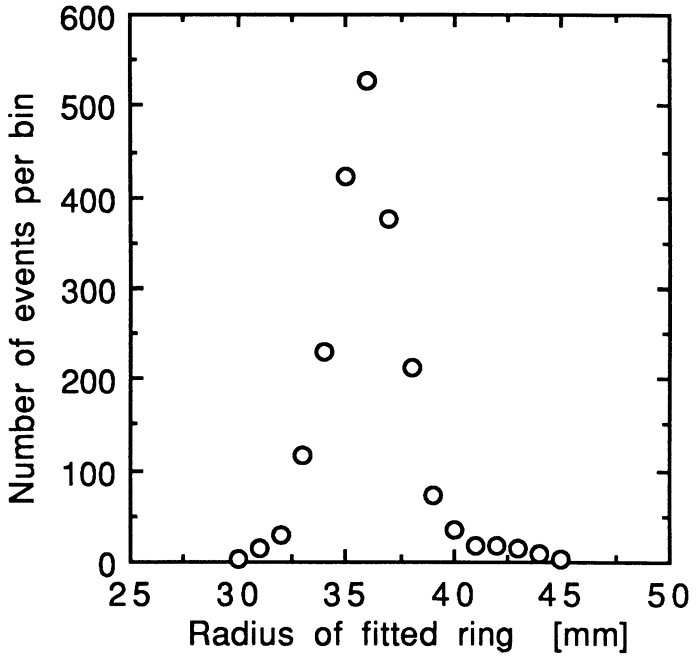


**Fig. 5** Distribution of ring radii calculated as "digital" centroids. Protons $\beta = 0.966$, TMAE at 40°C, HV = 1750 V, pad threshold 2 ADC ch., 2212 rings. The mean radius is 36.40 mm.

## 3. ANALYSIS OF THE RESULTS AND PERFORMANCE OF THE DETECTOR

The mean number of photo-electrons of a Cherenkov ring produced by a particle of velocity $\beta$, traversing a radiator of index n and thickness $L_0$, follows the relation:

$$N_{del} = N_0 \times L_0 \times \sin^2\theta, \quad (1) \qquad \text{with } \theta = \cos^{-1}(1/n \times \beta), \quad (2)$$

where $N_0$, the factor of merit, takes into account all sources of detection losses of photons and photo-electrons through the apparatus in use.

In order to discuss the performances of our detector, expressed by the factor of merit $N_0$, one has first to evaluate the number of detected photo-electrons, $N_{del}$, from the measured number of pads hit per ring, $N_{pad}$. Then, one should verify how the measurements satisfy the above relation after an evaluation of $N_0$ in our detection system. We present in sects 3.1 and 3.2 two simulation programs written in these purposes.

### 3.1 Model for generating a pad pattern of a ring

(a) The photonic processes not being considered for the moment, single electrons are generated inside the MWPC around a ring of known radius. Their number, $N_{iel}$, drawn from a Poisson distribution, is known; the centre of the ring is at a fixed point. For every electron, geometrical fluctuations are introduced, according to the known sources of error associated to our configuration: point of photon emission inside the radiator thickness, absorption point inside the MWPC gap and chromatic error. The azimuthal angle being randomly drawn, the position of every electron is known in the wire/pad frame of an experiment.

(b) From the work of Mathieson [4], an approximation of the normalized 3-D shape of induced charge has been calculated in our chamber geometry. Varying the position of the avalanche along the wire by steps of 0.5 mm over a pad width, a set of pad patterns is calculated which provides tables of weighting factors at every pad for different avalanche positions along the wire.

At every electron in a ring, a total charge is drawn from a distribution describing the avalanche process. In case of a single electron and low gain, that will be an exponential distribution of average $A_0$. Then, the pulse-height pad pattern of an electron is obtained by multiplying the total charge by the weighting pattern corresponding to the localization of this electron along the wire. Finally, the pulse-height pad pattern of a full ring is generated, taking into account pulse overlaps at any pad. The localization and the number of pad hit per ring are got by comparing this last pulse height pattern to a threshold $T_0$. The ring radius is calculated by various methods, analog, "digital" centroid, as well as other quantities such as multiplicities, single pad pulse-height spectra, etc.

(c) Finally, a factor, $eff_1$, ratio between the initial mean number of electrons per ring, $N_{iel}$, and the mean number of pads hit per ring, $N_{pad}$, can be calculated for different values of $A_0$, $T_0$, $N_{iel}$, radius, as well as $\varepsilon_{det}$, the mean efficiency of single-electron detection in a specific configuration. Figure 6 shows the variation of $eff_1$.

(d) In order to verify our model, the shape of the induced charge was measured by moving a well-collimated $55_{FE}$ source by steps along a wire. The result is compared to the model in fig. 7.

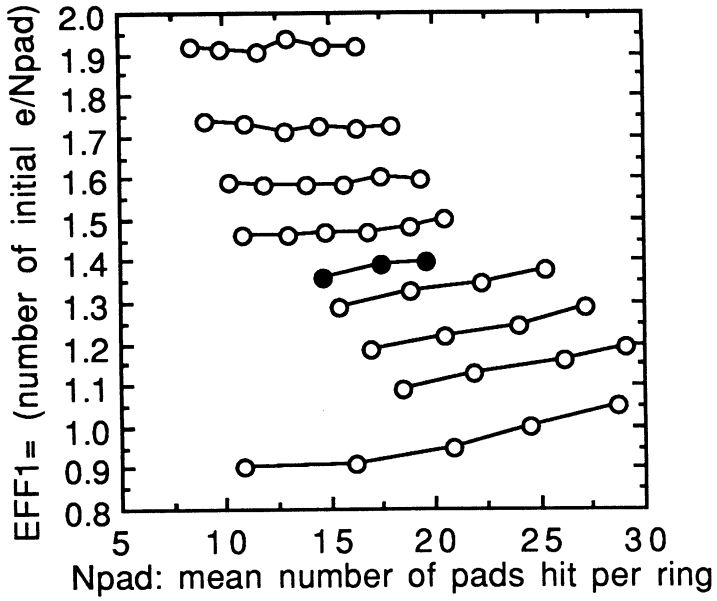


**Fig. 6** Variation of the factor, $eff_1$, giving, from the simulation, the number of initial photo-electrons corresponding to a measured number of pads hit above a threshold T (ADC ch.). The detection efficiency is not included in this value. $A_0$ (ADC ch.) is the mean value of the exponential pulse height (PH) distribution for single electrons used in the simulation. Open symbols, from top, $A_0$ = 3.5, 4.0, 4.5, 5.0, 5.5, 6.0, 7.0, 8.0, 10.0 ADC ch., T = 2 ADC ch., no FB photons. Full circles: 20% FB photons, $A_0$ = 4.5. The ring radius is 35 mm.

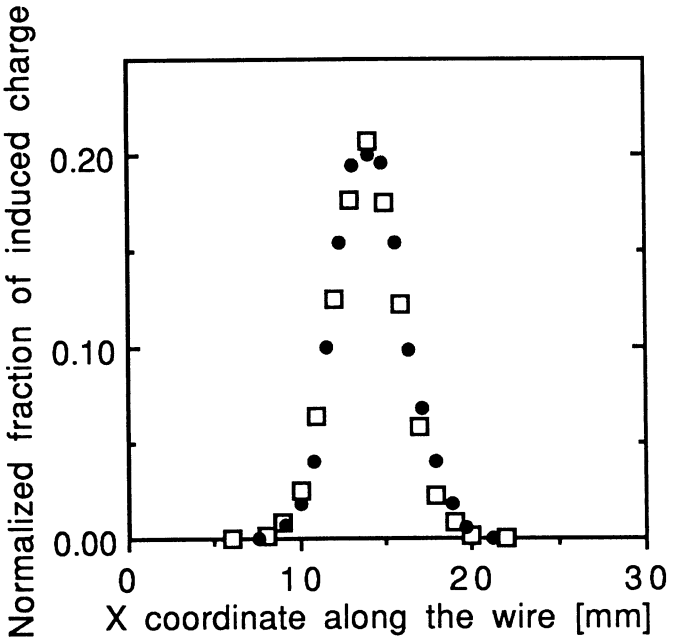


**Fig. 7** Measurement (square) of the spread of the induced charge compared to the simulation (circle). Pulse heights of hit pads above threshold are summed along columns perpendicular to the scanned sense wire. Pads of $4 \times 4$ mm$^2$, threshold 4 ADC ch., mean total pad pulse height (PH) 120 ADC ch.

It should be noticed that the detection efficiency of single electrons at low amplification depends upon the localization of the avalanche along the wire, as seen in fig. 8.

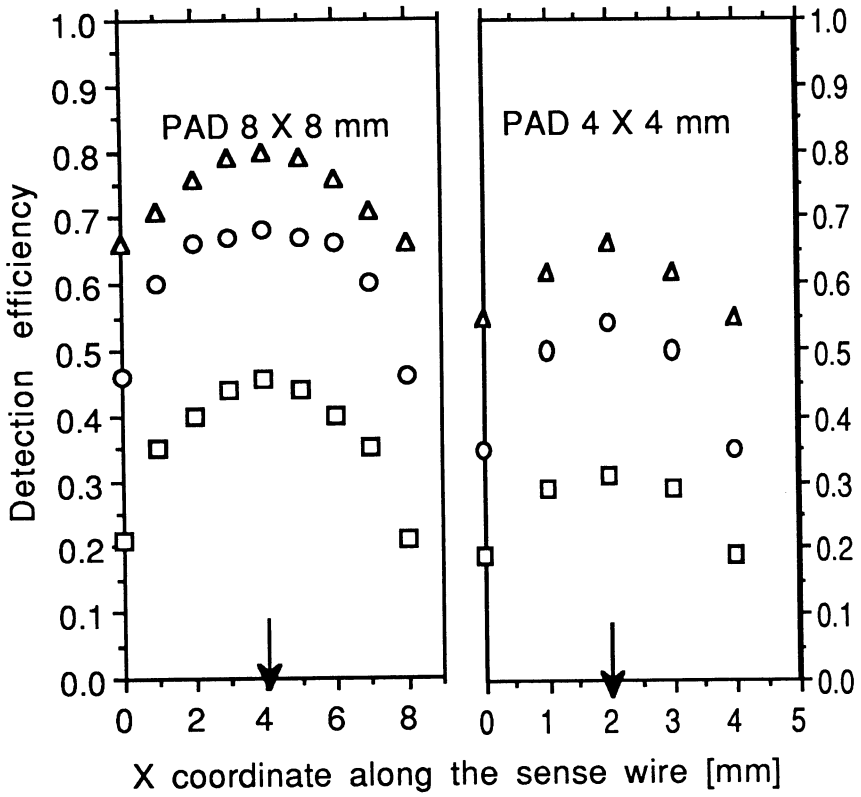


**Fig. 8** Calculated variation of the detection efficiency of a single electron versus its position along the sense wire in case of pad sizes of $8 \times 8$ mm$^2$ and $4 \times 4$ mm$^2$ (arrow = centre of the pad) and at different mean PH: from the top, $A_0$ = 12, 8, 4, thresh = 2.5 ADC ch.

### 3.2 Simulation of the factor of merit of a RICH using a solid radiator

Considering the detector geometry of fig. 1(a), the factors contributing to calculate $N_0$ are associated to the following processes:

(a) loss of photons coming from:
- the total reflection inside the radiator, $\varepsilon_{TR}$,
- the reflections at the interfaces NaF/helium, helium/quartz, quartz /MWPC, $\varepsilon_{refl}$,
- the absorption through the quartz window, $\varepsilon_{tr}$,
- the absorption through the mesh cathode, $\varepsilon_{gr}$,
- the absorption through the MWPC gas (TMAE), $\varepsilon_{abs}$;

(b) loss of electrons coming from:
- the TMAE quantum efficiency, $\varepsilon_{qe}$,
- the detection efficiency in the MWPC, $\varepsilon_{det}$.

$N_0$ is obtained by integrating these factors within a photon-energy window $\Delta E$:

$$N_0(\theta,E) = \int_{(\Delta E)} 370\ \varepsilon_{TR}(\theta)\ \varepsilon_{refl}(\theta)\ \varepsilon_{tr}(\theta)\ \varepsilon_{gr}(\theta)\ \varepsilon_{abs}(\theta)\ \varepsilon_{det}\ \varepsilon_{qe}(\lambda)\ dE \qquad (3)$$

The photonic loss factors, implying angles or trajectories through materials, depend upon the Cherenkov angle, that is, according to eq. (2), upon $\beta$ and the photon energy through the dispersion of the refractive index.

In a simulation program, photons of energy E, drawn in a flat distribution of width $\Delta E$, are followed through the detector array. The NaF index dispersion, the quartz transmission, the TMAE quantum efficiency curves and the TMAE absorption mean free path are introduced from the references quoted in the Appendix. Reflection losses and quartz transparency are calculated assuming a p polarization of the Cherenkov photons. A geometrical model provides an averaged mesh transparency at variable angles of incidence.

The mean number, nph, of photons emitted in the radiator necessary to generate a fixed number of electrons per ring, nel, in the MWPC is then calculated at a given $\beta$ and TMAE temperature, as well as efficiency coefficients following the sequence of every loss mechanism. The factor of merit is now given by

$$N_0 = 370\ \varepsilon_{det}\ \varepsilon_{gr}\ \text{nel}\ \Delta E/\text{nph}. \qquad (4)$$

Using the pad program described in sect. 3.1, a mean ring radius and its fluctuation is evaluated, providing a mean "effective" NaF index value at the corresponding $\beta$.

Referring to a set of the above-mentioned quantities listed in table 1, the main remarks, specific to the use of a NaF radiator, are the following:

**Table 1**

TMAE temp = 50°C, $\varepsilon_{det}$ = 1.0, nel = 20, $\Delta E$ = 2.63 eV (150–220 nm)

| Beta | $\varepsilon_{nph}$ | $\varepsilon_{TR}$ | $\varepsilon_{refl1}$ | $\varepsilon_{refl2}$ | $\varepsilon_{tr}$ | $\varepsilon_{refl3}$ | $\varepsilon_{gr}$ | $\varepsilon_{abs}$ | $\varepsilon_{qe}$ | $N_0$ |
|---|---|---|---|---|---|---|---|---|---|---|
| .815 | 179.4 | 1.0 | .994 | .985 | .608 | .981 | .778 | .734 | .260 | 84.4 |
| .845 | 169.4 | 1.0 | .997 | .992 | .607 | .990 | .764 | .764 | .259 | 87.6 |
| .875 | 157.1 | 1.0 | .999 | .998 | .608 | .997 | .748 | .803 | .262 | 92.7 |
| .905 | 153.9 | 1.0 | .993 | .996 | .610 | .999 | .728 | .844 | .255 | 92.1 |
| .935 | 151.7 | 1.0 | .969 | .978 | .626 | .995 | .697 | .883 | .252 | 89.4 |
| .950 | 150.6 | 1.0 | .941 | .953 | .649 | .988 | .673 | .906 | .255 | 87.0 |
| .965 | 159.4 | 0.941 | .897 | .929 | .721 | .973 | .644 | .922 | .247 | 78.6 |
| .980 | 171.3 | 0.820 | .880 | .911 | .809 | .951 | .605 | .940 | .245 | 68.8 |
| .995 | 201.7 | 0.702 | .853 | .888 | .906 | .920 | .557 | .959 | .233 | 53.7 |
| .9999 | 224.5 | 0.664 | .845 | .878 | .930 | .908 | .538 | .965 | .221 | 46.6 |

(a) Remind that the particle velocity determines a maximum index value below which photons can escape the radiator medium, that is, $n_{TR} = (1 + 1/\beta^2)^{1/2}$. As the NaF index can take values close to $\sqrt{2}$ at high-photon energy, a fraction of the Cherenkov radiation is expected to be cut-off in the high-energy range when $\beta$ approaches to 1. That is illustrated in table 1 by the decrease of $\varepsilon_{TR}$ when $\beta$ goes to 1. Let us notice that concurrently the quartz transparency increases as high energy photons are cut off. In fig. 9, the "effective" index values were calculated versus $\beta$ in detector configurations giving the same ring radius (35 mm) at a constant index (1.395). The index is found decreasing significantly in the 0.95–1 $\beta$ range. It means that a mean value of the index has to be calibrated as a function of the particle velocity $\beta$, depending upon the

materials in use in the set-up. Notice in table 1 the dependence, typical of that kind of set-up, of the factor of merit upon β.

Figure 10 shows energy spectra of the only converted photons at different β values.

**Table 2** β = 0.966, orthogonal tracks

| HV V | Temp. °C | $N_{pad}$ meas. | $A_0$ ADCch | $eff_1$ | $\varepsilon_{det}$ | $N_{del}$ meas. | $\varepsilon_{abs}$ | No $cm^{-1}$ | $N_{del}$ calcul. | $\Delta N/N_{del}$ % |
|---|---|---|---|---|---|---|---|---|---|---|
| 1700 | 50 | 23 | 5.0 | 1.52 | .55 | 19.2 | .922 | 43.2 | 19.2 | -0 |
| 1750 | 50 | 28 | 7.0 | 1.30 | .65 | 23.7 | .922 | 51.1 | 22.7 | +4 |
| 1700 | 40 | 17 | 3.7 | 1.83 | .46 | 14.3 | .783 | 30.2 | 13.4 | +7 |
| 1750 | 40 | 24 | 5.5 | 1.45 | .58 | 20.2 | .783 | 38.1 | 16.9 | +20 |
| 1800 | 40 | 31 | 8.5 | 1.13 | .70 | 24.5 | .783 | 46.0 | 20.4 | +20 |
| 1750 | 30 | 17 | 4.5 | 1.60 | .52 | 14.1 | .594 | 27.0 | 12.0 | +17 |
| 1800 | 30 | 22 | 6.5 | 1.28 | .63 | 17.7 | .594 | 32.8 | 14.5 | +22 |
| 1850 | 30 | 27 | 11. | 1.05 | .74 | 21.0 | .594 | 38.5 | 17.0 | +24 |

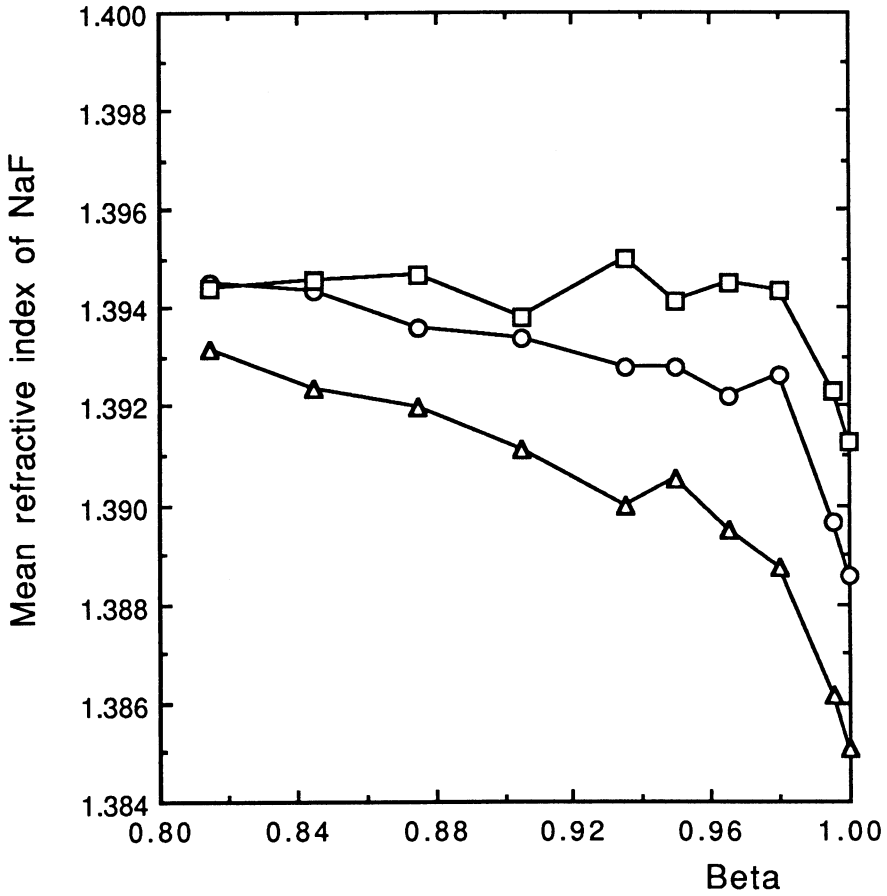


**Fig. 9** Simulation of the variation of the mean index of NaF versus β when all mechanisms of photon losses are taken into account within the wave-length range of 150–220 nm. Also shown is the influence of the mean free path of photo-absorption in TMAE, 4, 7, 12 mm (triangles, circles, and squares).

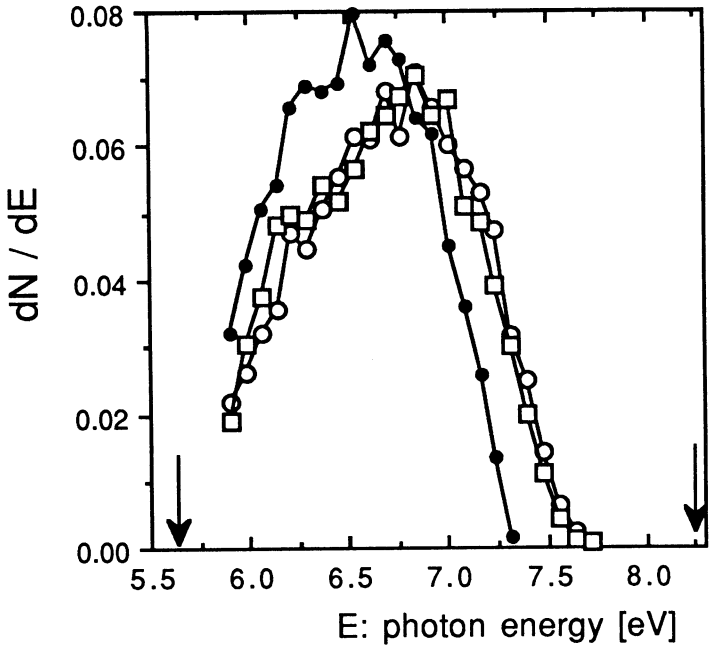


**Fig. 10** Energy distributions of those photons having traversed the detector and being converted in the MWPC, at three β values, circles: 0.845, squares: 0.950, dots: 0.9999.

(b) Taking this dependence into account, fig. 11 shows the contributions of the different loss mechanisms on the number of photo-electrons versus the particle velocity.

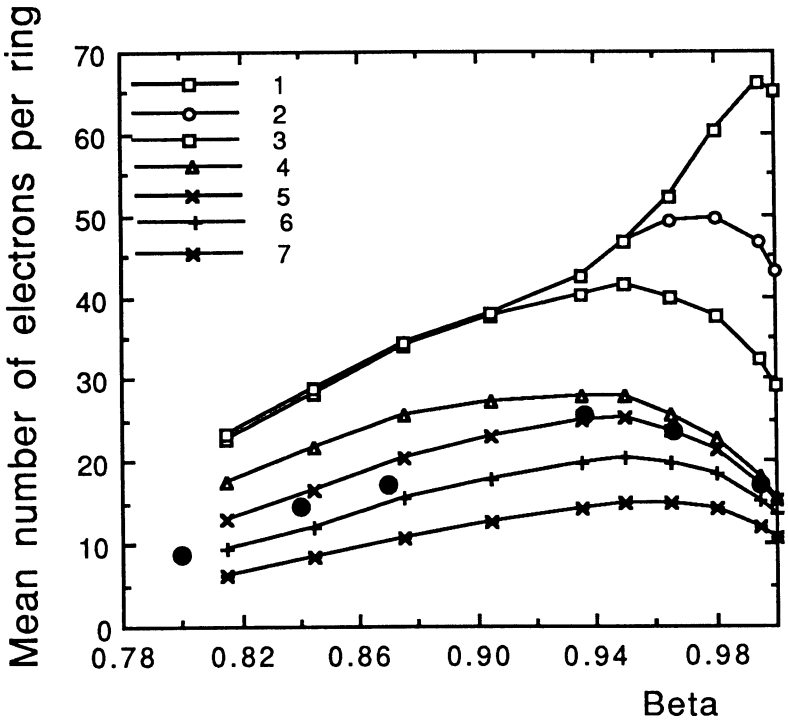


**Fig. 11** Number of detected photo-electrons versus particle velocity showing the cumulated influence of the various sources of photon losses.
From the top: $1 - \varepsilon_{q.e.}$ and $\varepsilon_{tr}$, $2 - \varepsilon_{TR}$, $3 - \varepsilon_{refl}$, $4 - \varepsilon_{gr}$, 5, 6, $7 - \varepsilon_{abs}$ at 4, 7, 12 mm mean free path. $\varepsilon_{det} = 0.68$.
$N_0$ values as a function of β are found for $\varepsilon_{det} = 1$ in table 1.
Full circles are measurements with TMAE at 50°C, HV = 1750 V.

# 4. DETERMINATION OF THE NUMBER OF PHOTO-ELECTRONS IN RINGS

Our simulation model (sect. 3.1) is runned for different numbers of initial photo-electrons with the following input parameters: the mean PH of single electrons, $A_0$, being measured independently at given TMAE temperature and HV, the pad threshold, the ring radius, known from the raw data, and the number of ring events in the analyzed run. A possible FB photon contribution is discussed later on. We get then the number of initial photo-electrons, $N_{iel}$, corresponding to the number of pads hit measured in this run ($eff_1$) and the mean detection efficiency, $\varepsilon_{det}$. We can write

$$N_{iel} = eff_1 \times N_{pad} \quad , \qquad N_{del} = \varepsilon_{det} \times N_{iel} \quad . \tag{5}$$

In addition, we generate the single pad PH distribution to be compared to the experimental ones.

The experimental number, $N_{del}$, is then compared to the one calculated according to the relations (1), (2) and (4) with the program described in sect. 3.2.

## 4.1 Photon feedback contribution: measurements with single electrons

We first examined the pulse height (PH) spectra obtained from single electrons generated in the detector with a well-collimated UV beam (deuterium lamp/suprasyl window). At every event, we sum the PH of all pads above threshold, keeping every signal within the linear dynamical range of the electronics.

As seen in fig. 12, they fit the expected exponential distribution until a certain level of voltage, $V_{fb}$. Above this value, an excess of events with respect to an exponential is found in the tail of the distribution, leading to a "convex" shape.

As shown in fig. 13, this is contradictory to the "concave" shape expected from simulated PH distributions where a fraction of the avalanches are initiated by 2 electrons. A possible cause, under investigation, might be found in a threshold effect on the pad readout generating discrete steps in the pad-signal summation. For the moment, we shall assume a fraction of an FB photon $< 20\%$ at $V > V_{fb}$, implying a 20% uncertainty in the determination of $A_0$ by fitting the experimental curve as a true exponential. In case of the more complex PH pattern of a Cherenkov ring, the same comparison will be made, now between a measured single-pad PH distribution and the simulation involving or not a known fraction of FB photons.

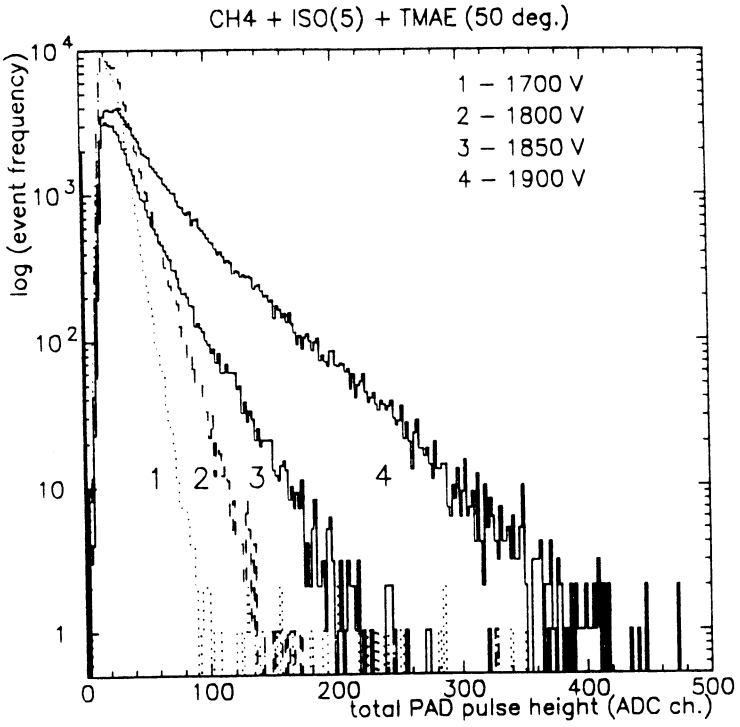


**Fig. 12** PH spectra of single electrons (UV beam) in methane 95%/isobutane 5%/TMAE 50°C, chamber at 60°C, at different voltages. The exponential lines are eye guides.

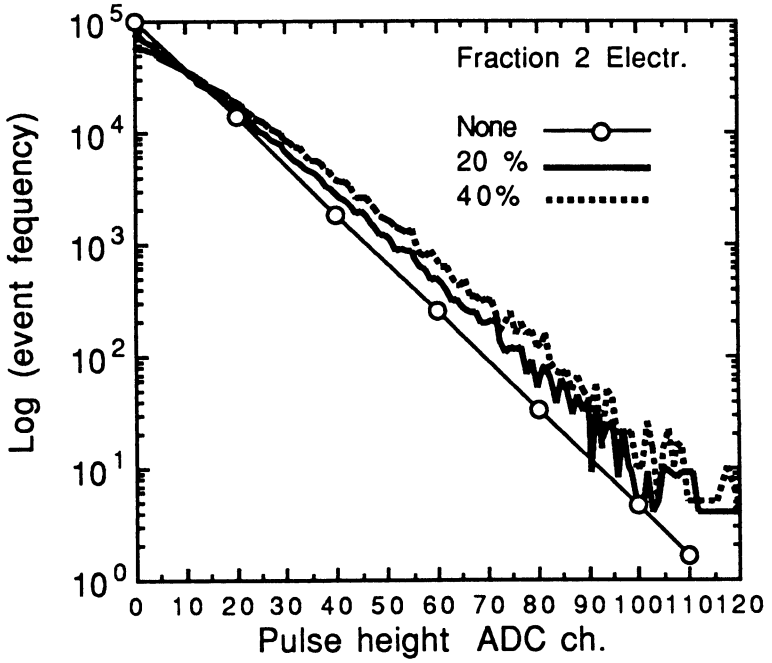


**Fig. 13** Simulated PH distribution of avalanches originated by one or two electrons: $A_0$ = 10 ADC ch. for a single electron avalanche.

We present in fig. 14 the measurements of the mean total pad PH from single-electrons obtained in different gas mixtures at different TMAE temperatures. The chamber

gain is evaluated at $5 \times 10^4$ at 1800 V, taking into account an integrating time of ≈ 300 ns of our electronics.

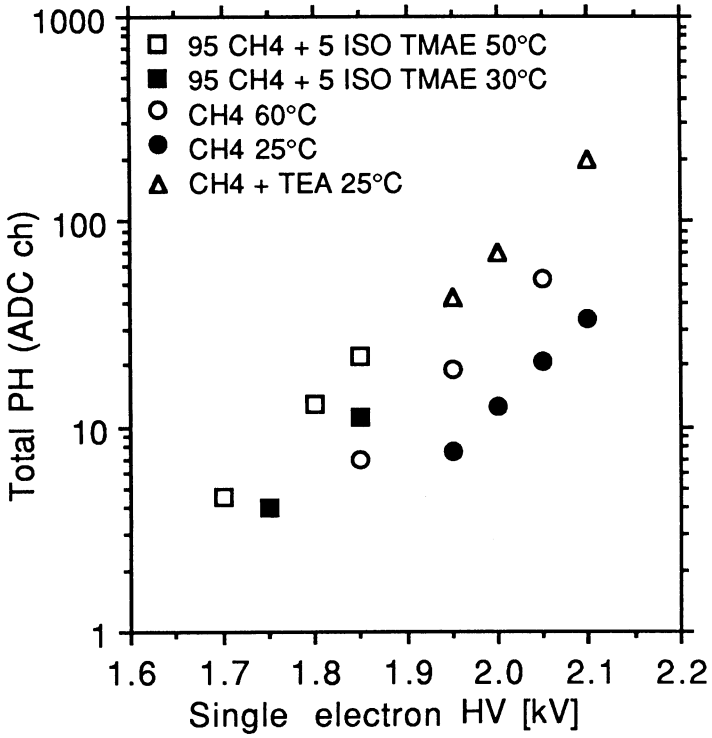


**Fig.14** Mean values of single-electron PH spectra measured in different gas mixtures and temperatures.

## 4.2 Results of the analysis and discussion

### 4.2.1 Factor of merit, comparison between data and simulation

In table 2 are assembled some results of measurements taken at different TMAE temperatures and chamber gains and the comparable quantities calculated according to our preceding assumptions.

Having chosen standard evaluations for the physical properties of the TMAE vapour, we observed that our measurements of the number of photo-electrons are found systematically 15–25% larger than the calculated ones at low TMAE temperatures (30°C and 40°C). Is this excess of electrons due to a contribution of FB photons?

Figure 15 compares a single pad PH spectrum measured at 50°C , where $N_{pad} = 28$, to different simulations. A first one, without FB photon contribution, leads to $N_{pad} = 27.4$ and a reasonable fit between the PH spectra. In the second one, introducing a contribution of 20% of FB photons, gives $N_{pad} = 28.3$, but a 15% decrease of $N_0$ and PH spectra now clearly separated. We never found a situation requiring an FB photon fraction > 10% to achieve simultaneously a good fit to the $N_{pad}$ value and the single pad PH spectra. However, the sensitivity of this procedure is still not accurate enough, due to the uncertainty on the $A_0$ determination. For the moment, we shall conclude that we cannot evaluate a photon FB contribution < 10% and take this value as a possible maximum in the experimental conditions of table 2.

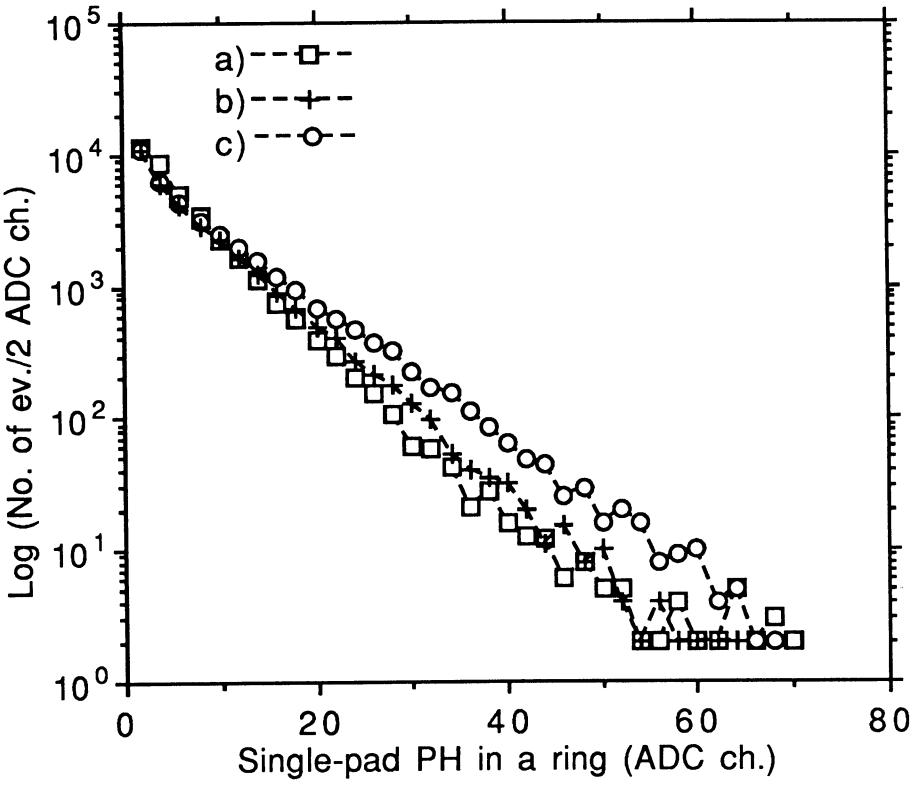


**Fig. 15** Spectrum of single-pad PH in a ring. Comparison between:
(a) A measured spectrum: TMAE at 50°C, HV = 1750 V, thresh = 2 ADC ch., 1200 rings,
(b) Its simulation without FB photons: $A_0$ = 7 ADC ch., thresh = 2 ADC ch., 1200 rings,
(c) Simulation of the influence of a fraction of 20% of events with FB photons.

If an extra source of electrons of a different origin than the FB photons has to be found, a possible assumption could be the contribution of an adsorbed layer of TMAE on the continuous pad electrode. That can be supported quantitatively by recent measurements [5], where efficiencies of ≈ 10% have been observed with such layers. It is also possible (as seen in fig. 2) that the MIP avalanches can also contribute.

Table 3 shows results where the particle velocity was varied at constant detection parameters.

**Table 3**

HV = 1750 V, TMAE temp. = 50°C, $A_0$ = 7 ADC ch., $\varepsilon_{det}$ = 0.65

| Beta | $N_{pad}$ meas. | $eff_1$ | $N_{del}$ meas. | $\varepsilon_{abs}$ | $N_0$ $cm^{-1}$ | $N_{del}$ calcul. | $\Delta N/N_{del}$ % |
|---|---|---|---|---|---|---|---|
| .800 | 11.5 | 1.15 | 8.6 | .735 | 54.8 | 10.7 | -24 |
| .840 | 19 | 1.18 | 14.6 | .772 | 57.0 | 15.3 | -5 |
| .870 | 22 | 1.20 | 17.1 | .797 | 60.2 | 19.1 | -11 |
| .936 | 30 | 1.32 | 25.7 | .886 | 58.1 | 23.8 | +8 |
| .966 | 28 | 1.30 | 23.7 | .922 | 51.1 | 22.7 | +4 |
| .995 | 22 | 1.20 | 17.1 | .968 | 34.9 | 16.5 | +4 |

As seen in fig. 11, the expected decrease of the number of photo-electrons is observed with a reasonable fit from $\beta = 0.80$ to 1, showing that a NaF radiator can still be used for tracks at normal incidence up to $\beta = 1$ with a quartz window. Let us notice that this apparatus could identify antiprotons of minimum kinetic energy of 0.4 GeV/$c^2$, of interest in some astrophysical applications.

### 4.2.2 Ring accuracy

Figure 16(a) shows the simulated variation of the ring accuracy versus $N_{del}$ when the chromatic contribution is not implemented in the calculation in order to evaluate the effect of the geometrical and pad detection errors. In this figure, the curve (a–1) represents in fact the intrinsic error due to the proximity focusing configuration. Such a result could be obtained with a detector achieving a very good two-dimensional localization of the photons, such as a multistep parallel plate counter. Spatial resolution values of $\approx 0.1$ per pad size, both for $2.6 \times 2.6$ and $7.6 \times 7.6$ mm$^2$ pads, have actually been realized in such counters built for the NA45 CERES experiment, using a particular analog centroid determination with simple geometrical scaling properties [6].

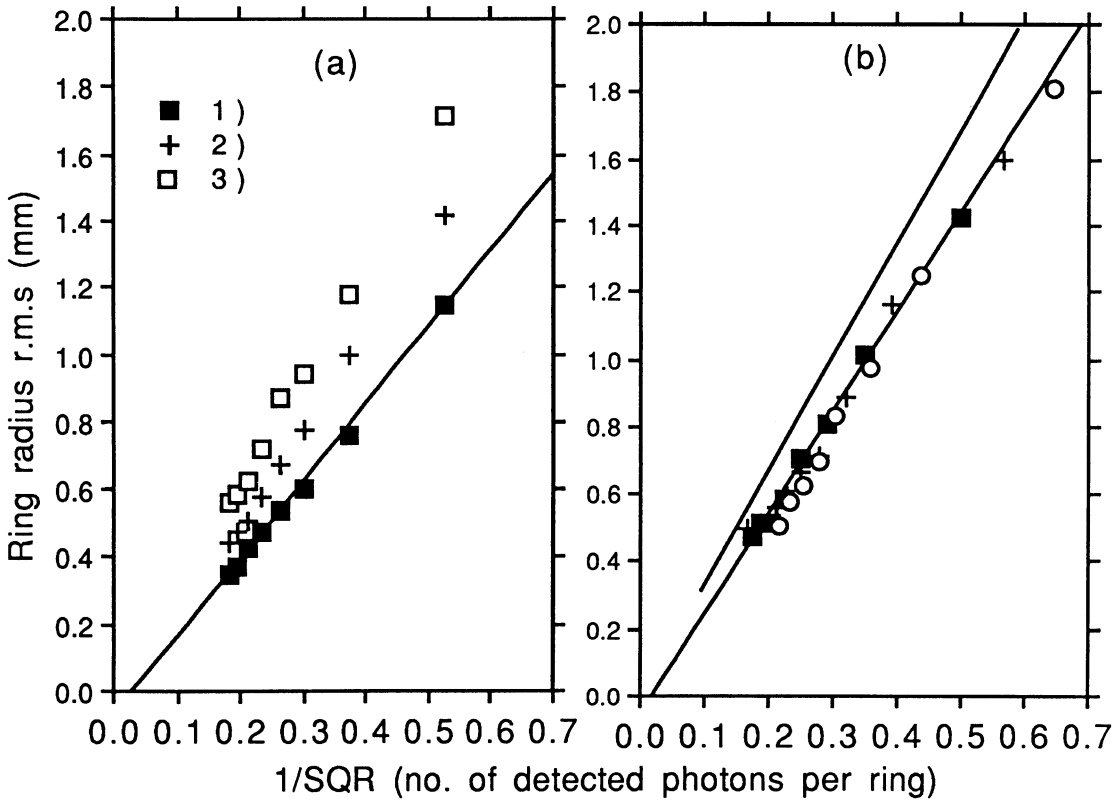


**Fig. 16** Simulated dependence of the accuracy of the ring radius versus the number of detected photo-electrons per ring, $N_{del}$.
(a) $A_0 = 10$ ADC ch., mean radius = 35 mm, pad $8 \times 8$ mm$^2$, pitch 4 mm. The errors on the localization of the photo-electrons are taken as in
1): only in the generation processes of photons (radiator) and electrons (MWPC); 2): same as 1) and best analog pad COG at thresh = 0, no pulse overlap; 3): same as 1) with digital pad COG at thresh = 2 ADC ch. and pulse overlap.
(b) $A_0 = 10$ ADC ch., mean radius = 35 mm, pad $4 \times 4$ mm$^2$, pitch 2 mm, digital pad COG at threshold = 1,2,3 ADC ch. The upper line is the fitted curve where pad = $8 \times 8$ mm$^2$ and pitch 4 mm.

In comparison to that minimum possible error, the digital centroid method (a–3) increases this number by a factor of ≈ 1.6 and an ideal analog centroid calculation (a–2) still by ≈ 1.3.

Figure 16(b) compares simulations of *digital* centroid finding in our set-up with a geometry: pad size of $4 \times 4$ mm$^2$ and wire pitch of 2 mm. A rather small improvement of the accuracy is obtained while the number of pads is multiplied by a factor of 4.

The geometrical uncertainty of the photo-conversion in the MWPC gap could be eliminated in a detection system using only adsorbed layers of TMAE on convenient material at the pad cathode. The quartz window could then eventually be suppressed at room temperature operation. Table 1 allows an evaluation of the gain in photon transmission, possibly balancing a lower quantum efficiency. Several development works are in progress in this domain.

In fig. 17, we show our ring accuracy measured with a NaF radiator and a calculation including now the chromatic error. A comparison is made with a freon $C_6H_{14}$ liquid radiator. Thanks to the lower index value and the smaller dispersivity of this liquid, the high-energy cut-off effect is now absent and the chromatic error reduced. The chromatic contribution of the NaF is then visible when compared to the freon radiator.

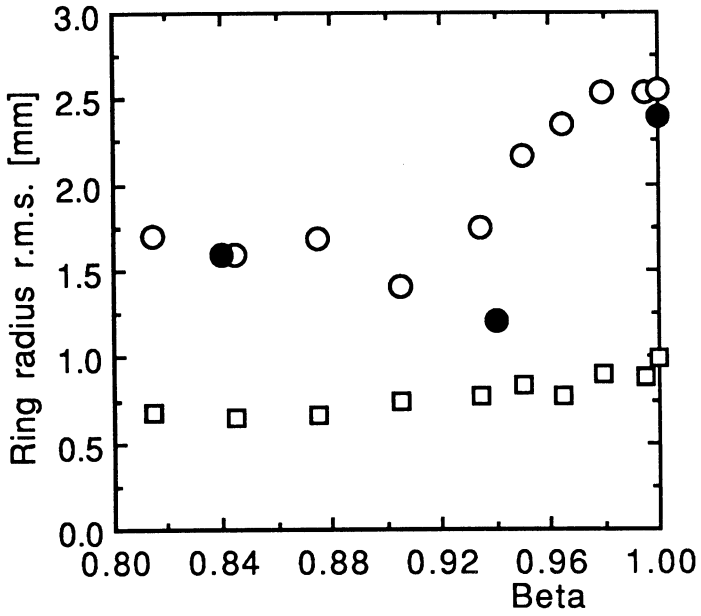


**Fig. 17** Ring accuracy. Open symbols: calculated with NaF (circles) and liquid freon (squares). Full symbols: measured with NaF radiator.

### 4.2.3 Particle separation

Figure 18 illustrates the reduction of the separation power due to the dependence of the "effective" refractive index with the particle velocity in case of a NaF solid radiator, according to fig. 9.

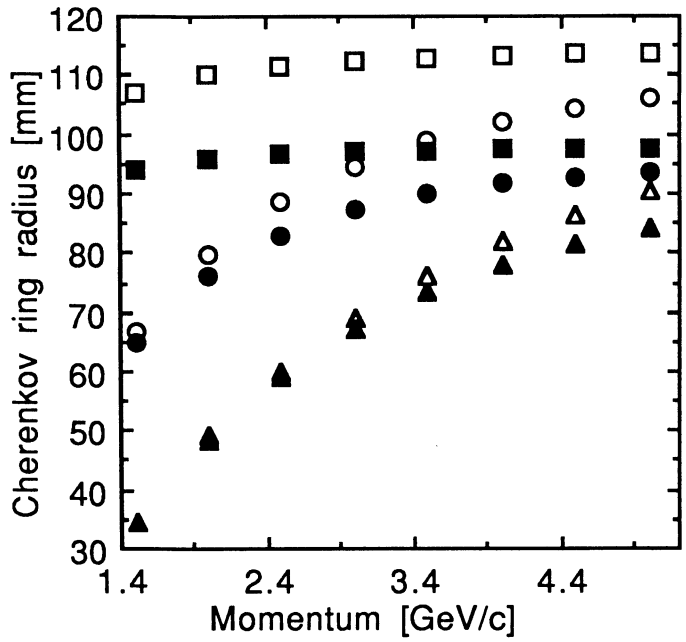


**Fig. 18** Separation power for pions (squares), kaons (circles) and protons (triangles). Ring radius as a function of the momentum calculated in the same detector geometry:

(a) open symbols: with a refractive index fixed at 1.393;

(b) full symbols: with a mean refractive index function of β.

For comparison, we show in fig. 19 what could be achieved with a liquid freon radiator. According to the preceding remarks, the lower index value reduces the separation power which could be compensated by a better accuracy. However, as an additional quartz window is necessary for liquid containment, ≈ 40% more Cherenkov photons are needed to obtain the same number of detected photo-electrons than with the NaF radiator. That may necessitate a chamber operation at higher gain to recover enough photo-electrons with the above-mentioned inconveniences.

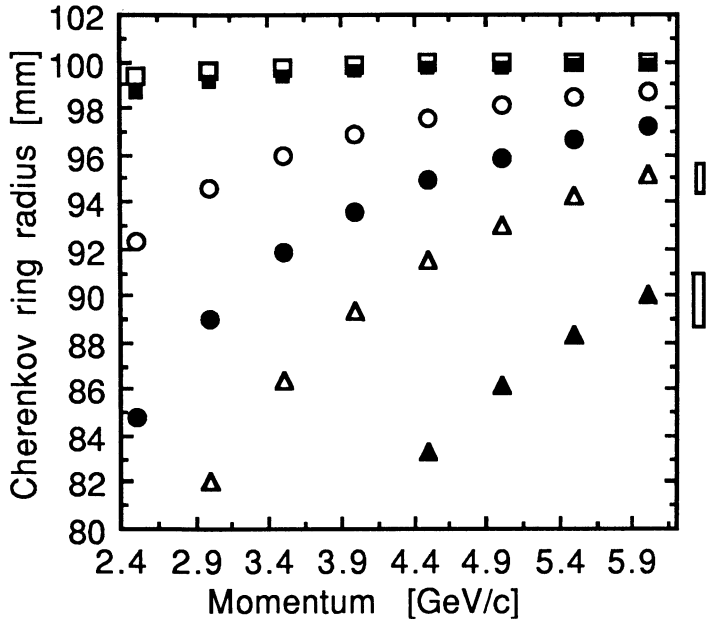


**Fig. 19** Separation power calculated in geometries giving the same ring radius for pions at β = 1. Pions (squares), kaons (circles) and protons (triangles). The 1 σ-resolution at β = 1 is indicated by rectangles:

(a) open symbols – liquid freon;

(b) full symbols – NaF.

These curves show that a ($3\sigma$) $\pi$/k separation could be achieved up to 4.0 GeV/c assuming a ring accuracy as in fig. 17.

### 4.2.4 Analog or digital measurements

Why, then, use an analog electronics in our particular case of a proximity focusing configuration if analog centroids are not essentially needed?

At the present time, we have only practical arguments. Handling very small signals renders a digital system difficult and expensive if electronic threshold uniformity has to be achieved on a large number of channels. Increasing the signal leads to increased gain or reduced gap which puts the load on the detector stability or feasibility. Analog electronics allows to set an individual threshold at every channel, defined at the software level from a pedestal/noise measurement [1]; that solves at low cost the gain spread problem. Access to the analog signal provides easier interpretation of the detector/electronics behaviour. In case of very high rate applications, digital solutions have well known advantages but pad structures are also interesting for possible sparse readout schemes benefiting from the local reduction of the event rate inherent to a two-dimensional readout.

### 4.2.5 Comparison with TEA and detector operation

We can compare in fig. 14 single-electron PH measurements obtained in TEA or TMAE mixtures. Our previous measurements [1] showed that similar numbers of pads hit per ring were obtained in TEA at a voltage of 2000 V, $CaF_2$ window, compared to 1750 V and quartz window in TMAE. That represents a factor of $\approx 10$ in the chamber gain. In addition, a higher threshold had to be applied on PH pad data in order to decrease the spread of induction of the MIPs. One has then to balance between a certainly more risky long-term operation at high gain, expensive windows but room temperature set up in case of TEA and lower gain at 30–50°C in case of TMAE.

Our chambers were operated without any problems at beam rates of 1–2 kHz/wire, temperature up to 70°C, for long run periods. However, we have not yet results about ageing or chemical effects to be reported.

## 6. CONCLUSIONS

We presented the study of a fast RICH detector with a proximity focusing geometry made of a solid radiator and, as photodetector, a symmetric MWPC of 4 mm thickness. Photo-electrons and particles are localized by measuring the charges induced at a cathode segmented into pads of $8 \times 8$ mm$^2$, with the help of a VLSI detection electronics of sensitivity 2500 electrons e.c. Using as photo-converting vapour TMAE at 30 – 50°C in 95 methane/5 isobutane, up to 24 electrons per ring are detected (factor of merit of

58 $cm^{-1}$) at a chamber gain not much than $5 \times 10^4$. Comparison to a simple model and measurements on single electrons indicates negligible amount of feedback photons although an excess up to 25% in the number of photo-electrons is found using standard values of quantum efficiency and photon mean free path. To account for this excess, the assumption of an adsorbed TMAE layer at the plane cathode is being tested. A maximum accuracy of 1.3 mm on the Cherenkov ring radius is achieved by using a "pad digital centroid" determination of this radius. It has been found that the use of a NaF radiator associated with quartz windows implies a correction factor on the mean refractive index as a function of the particle velocity, influencing significantly the separation power of this detector. A $3\sigma$ $\pi$/k separation seems possible up to 4 GeV/c with the present level of ring accuracy.

These tests have demonstrated that a fast RICH structure of simple and cheap manufacturing can be envisaged for large detection areas allowing for high factor of merit at low gain, two-dimensional readout and fast resolving time between events.

## Acknowledgements

We thank E. Bianchi and R. Alberganti for their excellent work in the design and manufacturing of the electrodes and all variety of electronics boards. We are also indebted to E. Heijne and P. Jarron for many discussions and advices in the field of AMPLEX.

One of the authors (MS) gratefully acknowledges financial support by CERN and the Institute of Nuclear Physics Democritos, Athens, Greece.

## APPENDIX

**A1.** The dispersion curve of the refractive index of NaF can be fitted to measurements [7], using the Sellmeier formula

$$(n^2 - 1)/(n^2 + 2) = F_1/(E_1^2 - E^2)$$
with $F_1 = 48.76\ eV^2$, $E_1 = 15.78\ eV$ [8].

The dispersion curves of liquid freon, $C_6F_{14}$, and quartz are taken from ref. [9], respectively as

$$n = 1.2177 + 0.00928\ E,$$

$$n^2 - 1 = F_1/(E_1^2 - E^2) + F_2/(E_2^2 - E^2) \text{ with } F_1 = 46.411\ eV^2,$$

$$E_1 = 10.666\ eV,\ F_2 = 228.71\ eV^2,\ E_2 = 18.125\ eV.$$

E is the photon energy expressed in [eV].

**A2.** The UV transmission curve of the Suprasil window is obtained by fitting measurements taken at different quartz thicknesses x [mm]:

$$\varepsilon_{tr}(x,\lambda) = \exp\{D - x\ (\lambda^{-A}\ \exp[B - \lambda\ C])\}/100$$
with $A = 7.8627$, $B = 62.4$, $C = 0.13849$, $D = 4.52$,
where $\lambda$ lies in the range 150–220 nm.

**A3.** The TMAE quantum efficiency curve is a fit to the Seguinot's measurement within a photon-energy window of 150–220 nm [10].

**A4.** The TMAE mean free path of absorption, according to ref. [11], is taken as 4, 7 and 12 mm respectively at 50, 40, 30°C.

## REFERENCES

[1] E. Chesi et al., Nucl. Instr. and Meth. A283 (1989) 602.

[2] E. de Beuville et al., Nucl. Instr. and Meth. A288 (1990) 157.

[3] E. Chesi et al., CERN/EF Internal Note (1989).

[4] E. Mathieson et al., Nucl. Instr. and Meth. 227 (1984) 277.

[5] V. Dangendorf et al., Weizmann Institute, WIS 89/81/Dec/Ph. (1989);
J. Séguinot et al., CERN/EP 90–88, submitted to Nucl. Instr. and Meth. (1990).

[6] H. Specht, CERES/NA45, private communication.

[7] A. Smakula, US Department of Commerce, Office of Technical Services, Document 111052 (1952) 88.

[8] R. Arnold et al., Nucl. Instr. and Meth. A273 (1988) 466.

[9] T. Ypsilantis, preprint CERN/EP 89–150 (1989).

[10] R.A. Holroyd et al., Nucl. Instr. and Meth. A261 (1987) 440;
J. Séguinot, CERN/EP 89–92, LPC/89-25 (1989).

[11] R. Chechik et al., Nucl. Instr. and Meth. A264 (1988) 251.

Imprimé au CERN. Prix : 0.90 Fr.